ACS OMEGA

Article

Cite This: ACS Omega 2019, 4, 10129−10139

http://pubs.acs.org/journal/acsodf

Borohydride-Assisted Surface Activation of $Co_3O_4/CoFe_2O_4$ Composite and Its Catalytic Activity for 4-Nitrophenol Reduction

Jose-Luis Ortiz-Quiñonez and Umapada Pal*

Instituto de Física, Benemérita Universidad Autónoma de Puebla, Apartado Postal J-48, 72570 Puebla, Pue., México

Supporting Information

ABSTRACT: Surface activation of catalysts is known to be an efficient process to enhance their activity in catalytic processes. The activation process includes the generation of oxygen vacancies, changing the nature of the catalyst surface from acidic to basic and vice versa, and the reduction of catalyst surface by H_2. On the other hand, magnetically separable catalysts are highly beneficial for their utilization in water or biological fluid-based catalytic processes, as they can be easily guided to the target site and recovered. Here, we present the fabrication of $CoFe_2O_4$ and composites of $Co_3O_4/CoFe_2O_4/\alpha$-Fe_2O_3 and $Co/CoFe_2O_4/\alpha$-Fe_2O_3 through solution combustion process to utilize them as catalysts for 4-nitrophenol (4-NP) reduction. Although none of the as-prepared $CoFe_2O_4$ and $Co_3O_4/CoFe_2O_4$ was seen to be active in 4-NP reduction reaction, the surface of the composite gets activated by borohydride ($NaBH_4$) treatment to act as a highly active catalyst for 4-NP reduction. X-ray photoelectron spectroscopy of the composite revealed the formation of metal-hydroxide (M−O−H) species of both Co and Fe at its surface due to borohydride treatment. The mechanism of the surface activation and the dynamics of 4-NP reduction of the surface-activated composite have been studied, proposing a possible pathway for the reduction of 4-NP.

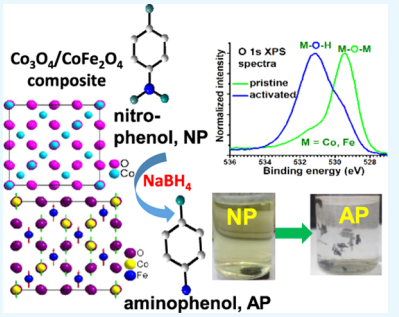

1. INTRODUCTION

Transforming nitroarenes into anilines is of great importance as anilines are among the most important intermediates used for the production of dyestuffs and pharmaceuticals.[1] 4-Nitrophenol (4-NP) is a toxic nitroarene, generated as a byproduct in the production of pesticides, synthetic dyes, leather preservative, and as intermediate in the production of paracetamol.[2,3] Furthermore, the reduction of 4-NP is a well-known model system commonly used to test the catalytic behaviors of metals and other materials that can reduce organic molecules.[4] To achieve 4-NP reduction, noble and non-noble metals have been frequently utilized as catalysts.[2,3,5] The inconveniences of using metals in these chemical reactions are the lack of selectivity in the reduction of nitroarenes and the high cost of noble metals (e.g., Au, Pt, Ru, Pd).

To address these inconveniences, metal/metal oxide composites have been investigated for the reduction of $-NO_2$ group in nitroarenes. High selectivity of Ni/TiO_2 or Au/TiO_2 composites for the reduction of nitroarenes has also been demonstrated.[6] The high selectivity was attributed to the bonding of $-NO_2$ group of 4-NP with metal oxides.[6] Likewise, hydrogenated MoO_x (H-MoO_x) loaded with bimetallic Pt−Sn (Pt−Sn/H-MoO_x) has also been utilized to hydrogenate 4-nitrostyrene.[7]

However, very few cobalt ferrite ($CoFe_2O_4$) or composites based on $CoFe_2O_4$ have been tested so far as catalysts for the reduction of 4-NP.[8,9] Some works claim that $CoFe_2O_4$ reduce the 4-NP, but the signal-to-noisy ratios in their X-ray diffraction (XRD) patterns were low, therefore, there is a possibility that the undetected impurities present in a small amount might be responsible for their catalytic activity.[10−12] One advantage of using $CoFe_2O_4$-based composites as catalysts is that they are magnetically separable. Cobalt ferrite ($CoFe_2O_4$) is an interesting ferrimagnetic material that has a high saturation magnetization.[13] Although metal oxides such as NiO and CuO have been utilized by several research groups as catalysts for the reduction of 4-NP,[14] rarely the catalysts have been analyzed by X-ray photoelectron spectroscopy (XPS) before and after their utilization in 4-NP reduction. The high-resolution spectra obtained by this technique provide relevant information regarding the chemical composition, oxidation states, adsorbed ions, and other characteristics of the oxide surfaces that can shed light on the nature of the catalyst surface required for the reduction of 4-NP.

On the other hand, during the synthesis of cobalt ferrite ($CoFe_2O_4$) nanoparticles by the solution combustion reaction, frequently small amounts of superparamagnetic (e.g., Co nanoparticles), nonmagnetic (e.g., α-Fe_2O_3, Co_3O_4, CoO), and amorphous byproducts are generated over their surfaces.[15] These byproducts might also be catalytically active in the reduction of 4-NP. In particular, the purity and size of the cobalt ferrite particles obtained using a solution combustion process depend on several factors such as: (i) oxidizing and reducing agent ratio,[16] (ii) annealing temperature, and (iii) annealing time. Apart from α-Fe_2O_3, CoO, and Co_3O_4, the generated byproducts can also contain the clusters or particles

Received: January 14, 2019
Accepted: May 13, 2019
Published: June 11, 2019

of cobalt, iron oxohydroxydes (e.g., FeOOH), amorphous materials, etc.,[10,12] the catalytic behaviors of which are unknown. Furthermore, a small amount of some of these byproducts may be detected through their catalytic activities, which is a relevant issue for applications in which pure $CoFe_2O_4$ is required. The utilization of $CoFe_2O_4$ as a heterogeneous catalyst has been reported in the literature,[17] and the strategy of using $CoFe_2O_4$ as a catalytic support is of great advantage due to its high chemical stability.

In the present work, we demonstrate that phase pure $CoFe_2O_4$ particles are not at all active as catalyst for the reduction of 4-NP. However, some byproducts such as Co_3O_4 generated during the preparation of $CoFe_2O_4$ particles by the solution combustion reaction manifest high catalytic activity after activating their surface with $NaBH_4$ for about 4 h. The Co_3O_4-supported $CoFe_2O_4$ composites could be prepared by a low-temperature solution combustion process, controlling the nitrate ions/glycine (N/G) ratio in the reaction mixture. We demonstrate that the magnetic composite can be activated by $NaBH_4$ during the reduction of 4-NP to 4-aminophenol, through the formation of metal hydroxides at its surface. The mechanism of surface activation and the reduction of 4-NP have been extensively studied utilizing X-ray photoelectron spectroscopy.

2. RESULTS AND DISCUSSION

2.1. XRD Results. Figure 1 presents powder X-ray diffraction (XRD) patterns of the cobalt ferrites prepared at four different N/G ratios. As can be seen in Figure 1a,b, $CoFe_2O_4$ prepared at N/G ratios 6 and 4.5 are in the phase pure spinel structure, and all their diffraction peaks coincide in intensity and position with the standard values reported in the PDF #4-006-4147. However, for the sample prepared at N/G ratio 3.0, there appeared a small peak at $2\theta = 33°$ associated to the (104) plane (PDF # 00-033-0664) of α-Fe_2O_3. On the other hand, the sample prepared at a N/G ratio 2.0 revealed several diffraction peaks associated to α-Fe_2O_3 and Co_3O_4 (Figure 1d), confirming the formation of α-Fe_2O_3 and Co_3O_4 impurities during the synthesis of $CoFe_2O_4$ at lower N/G ratios. The two small diffraction peaks located at $2\theta = 31.27$ and 36.84° (indicated with the diamond symbols in Figure 1d) coincide in position with the (220) and (311) planes of Co_3O_4 in the cubic phase (PDF #04-005-4386). Formation of these two impurities is associated to the higher temperature and intense flame generated during the combustion reactions occurred for the N/G ratios 3.0 and 2.0. Unfortunately, owing to the fluorescence in the XRD patterns generated by the cobalt containing compound, it was not possible to estimate the particle/grain size of these byproducts from their XRD peaks.

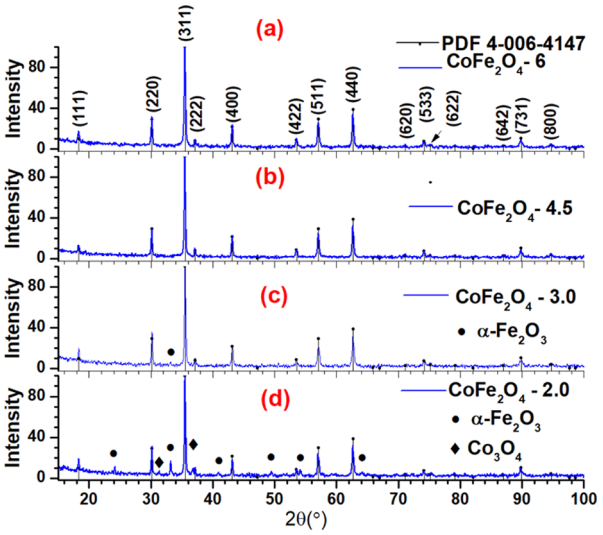

Figure 1. XRD patterns of $CoFe_2O_4$ particles synthesized at different N/G ratios. (a) N/G: 6, (b) N/G: 4.5, (c) N/G: 3.0, and (d) N/G: 2.0.

Figure 2 depicts the X-ray patterns of selected samples in the $2\theta = 30-53°$ range with an enhanced signal-to-noise ratio (compared to Figure 1). As can be noticed, the presence of cobalt nanoparticles could be detected in the $CoFe_2O_4$-3.0 sample from its diffraction pattern. The position of the diffraction peaked located around 44.30° matches perfectly with the position of the most intense diffraction peak of metallic cobalt (PDF # 00-015-0806). In addition, the diffraction peak located at $2\theta = 36.97°$ in Figure 2 associated to the (222) plane of Co_3O_4 is better resolved than its peak appeared in Figure 1. For comparison, the XRD pattern of Co_3O_4 is presented in Figure S1.

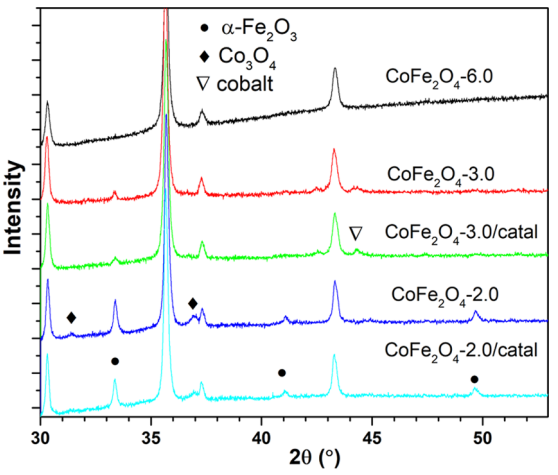

Figure 2. Slow-scanned XRD patterns of $CoFe_2O_4$ particles synthesized at different N/G ratios: 6.0, 3.0, and 2.0 in the $2\theta = 30-53°$ range. XRD patterns of the impure samples prepared with the ratios 3.0 and 2.0 are also included after being used as a catalyst.

2.2. Scanning Electron Microscopy (SEM). Typical SEM images of the $CoFe_2O_4$ particles prepared at four N/G ratios are presented in Figure 3. It can be seen that the $CoFe_2O_4$-6.0 and $CoFe_2O_4$-4.5 samples are composed of sub 100 nm particles, highly agglomerated due to the post-growth annealing at 600 °C. Interestingly, the $CoFe_2O_4$-3.0 and $CoFe_2O_4$-2.0 samples contain a good fraction of particles larger than 400 nm that were not found in the SEM images of the samples prepared at N/G ratios 6.0 and 4.5. These larger particles were generated in these samples as a result of the decomposition of NO_3^-, and glycinate ($H_2NCH_2COO^-$) ions at high temperature reached inside the mixture under the intense flame. Consequently, the particles prepared at N/G ratios 3.0 and 2.0 grown faster during their annealing than the particles in samples prepared at N/G ratios 6.0 and 4.5. A common feature of these larger particles (Figure 3c,d) is their smooth facets.

DOI: 10.1021/acsomega.9b00118
ACS Omega 2019, 4, 10129−10139

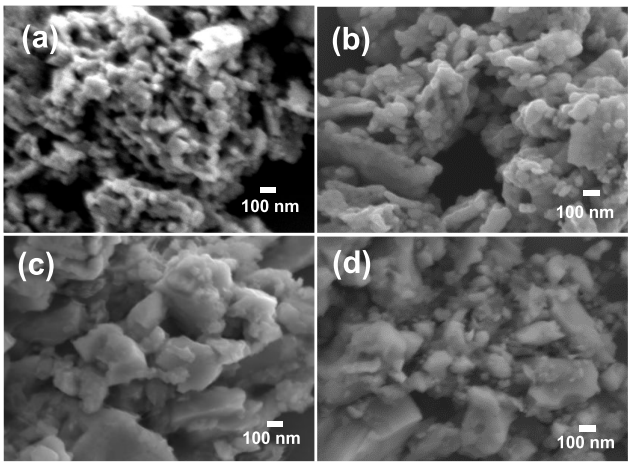

Figure 3. Typical SEM images of the (a) $CoFe_2O_4$-6.0, (b) $CoFe_2O_4$-4.5, (c) $CoFe_2O_4$-3.0, and (d) $CoFe_2O_4$-2.0 samples.

Elemental mapping of the samples $CoFe_2O_4$-6.0, $CoFe_2O_4$-4.5, $CoFe_2O_4$-3.0, and $CoFe_2O_4$-2.0 are shown in Figures S2–S5 in the Supporting Information. The results confirmed that the constituent elements are distributed homogeneously in $CoFe_2O_4$. However, in Figure S5a, there appeared a zone in the sample (indicated by an arrow) where the amount of cobalt is lower than expected (Figure 4Sb). That zone could be a region of the sample containing the byproduct α-Fe_2O_3 previously detected in the XRD pattern.

2.3. N_2 Adsorption–Desorption Isotherms and Surface Area. N_2 adsorption–desorption isotherms of the cobalt ferrite samples recorded at 77 K are shown in Figure 4. As can be seen, although the sample $CoFe_2O_4$-6.0 exhibits type-II isotherm, the isotherms of the samples $CoFe_2O_4$-4.5, $CoFe_2O_4$-3.0, and $CoFe_2O_4$-2.0 are the mixture of type-II and type-IV. Although type-II isotherms are obtained for nonporous or macroporous adsorbents, type-IV isotherms contain hysteresis loops and are characteristic of mesoporous materials.[18] As we can see, for the $CoFe_2O_4$-6.0 sample, the adsorption and desorption branches of the isotherm almost coincide, which is the characteristic of a macroporous solid. In fact, some macropores in the $CoFe_2O_4$-6.0 sample were observed in its SEM image (Figure 3a). On the contrary, the isotherms for the $CoFe_2O_4$-4.5, $CoFe_2O_4$-3.0, and $CoFe_2O_4$-2.0 samples revealed hysteresis loops, which are associated to the capillary condensation inside the mesopores. The capillary condensation might have occurred in the voids of aggregated particles. Only for the $CoFe_2O_4$-4.5 and $CoFe_2O_4$-3.0 samples, the adsorption–desorption branches split at low pressure (p/p_0 = 0.3), indicating the initiation of the capillary condensation in these samples at lower pressure.

The specific surface area of the samples was calculated using the Brunauer–Emmett–Teller (BET) equation

$$a_s = \frac{V_m}{22\,414} \times L \times \sigma$$

where V_m is the monolayer volume, L is the Avogadro constant, and σ is the cross-sectional area of the N_2 molecule (0.162 nm^2). Although the largest surface area was estimated for $CoFe_2O_4$-6.0, the second largest area was obtained for the $CoFe_2O_4$-4.5 sample (see Table 1). On the other hand, the $CoFe_2O_4$-3.0 and $CoFe_2O_4$-2.0 samples had very low surface areas, as expected for the samples containing larger particles (Figure 3c,d). The large difference in surface area is due to the intense flame generated during the combustion in the synthesis of the later samples. As can be recalled, although there appeared no or low flame during the combustion for the samples prepared at N/G ratios 6.0 and 4.5, intense flames were generated for the samples prepared at N/G ratios 3.0 and 2.0. Consequently, the nitrate species were not fully decomposed during the combustion reaction in the case of N/G ratios 6.0 and 4.5. Instead, they were decomposed during

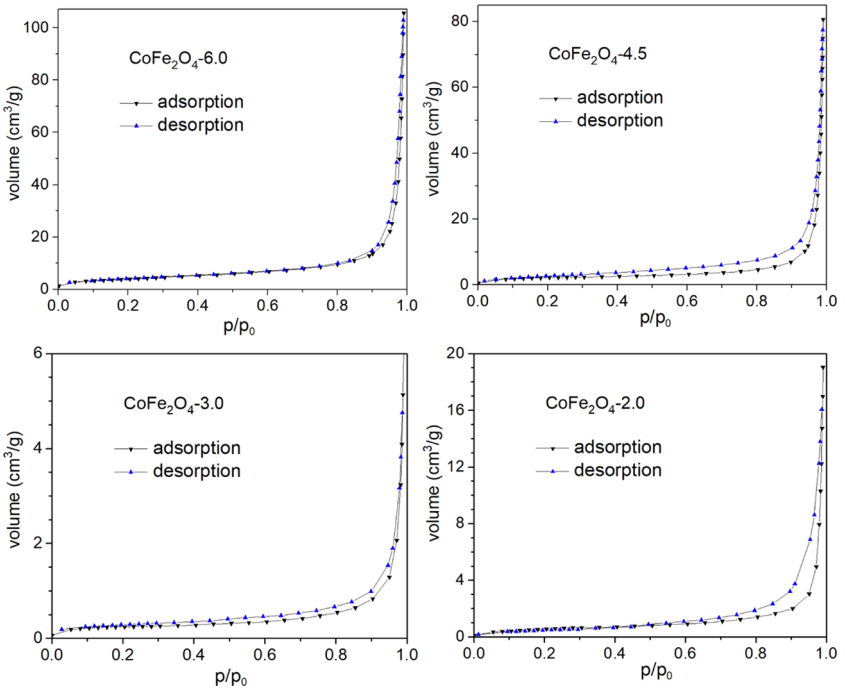

Figure 4. N_2 adsorption–desorption isotherms of cobalt ferrites synthesized at N/G ratios 6.0, 4.5, 3.0, and 2.0.

DOI: 10.1021/acsomega.9b00118
ACS Omega 2019, 4, 10129–10139

Table 1. Texture Parameters of $CoFe_2O_4$ Samples[a]

sample	a_s (m^2/g), BET	C	total pore volume (cm^3/g), BET	pore volume (cm^3/g), BJH-ads	pore area (cm^2/g), BJH-ads
$CoFe_2O_4$-6.0	14.422	86.384	0.160	0.159	14.116
$CoFe_2O_4$-4.5	7.556	169.47	0.124	0.123	6.053
$CoFe_2O_4$-3.0	0.841	376.24	0.00857	0.00840	0.6057
$CoFe_2O_4$-2.0	2.064	39.476	0.0277	0.0275	2.043

[a] a_s represents the specific surface area of the samples. C is approximately equal to $\exp\{(E_1 - E_L)/RT\}$, where E_1 = heat of adsorption of the first N_2 layer, E_L = heat of liquefaction of N_2, R = constant of the gases, and T = temperature.[19]

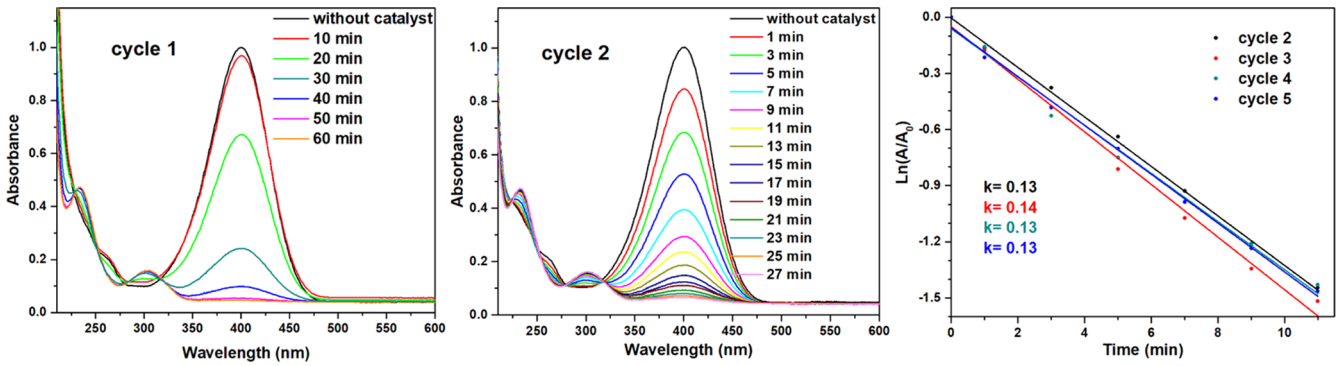

Figure 5. UV−vis absorption spectra corresponding to the progressive reduction of 4-nitrophenol to 4-aminophenol using $CoFe_2O_4$-3.0 sample as a catalyst. Cycle 2 corresponds to the first reusability test.

the after-growth annealing, which is a slower growth and sintering process.

Pore volume and pore area in the samples were also estimated by the Barrett−Joyner−Halenda (BJH) method using the adsorption branch of the isotherms and presented in Table 1. It can be noted that the total pore volume determined using both the BET and BJH methods is very similar for all of the samples.

2.4. Catalytic Activity. The catalytic reduction of 4-NP was tested for all of the four samples. The degradation of 4-NP was not observed for the $CoFe_2O_4$-6.0 and $CoFe_2O_4$-4.5 samples within the first 10 cycles (results presented in Figure S6 for the $CoFe_2O_4$-4.5 sample). Since for these two samples, only the $CoFe_2O_4$ phase was detected through the XRD analysis, we can conclude that the phase pure cobalt ferrite does not reduce 4-NP. However, the $CoFe_2O_4$-3.0 sample reduced all of the 4-NP to 4-AP in the first cycle and also in its subsequent reusability tests. The reduction of 4-NP to 4-AP could be affirmed from the progressive reduction of the intensity of the absorption band at 400 nm, characteristic of 4-NP, after the addition of $NaBH_4$, and a subsequent growth of the 300 nm absorption band associated to the 4-aminophenol (4-AP) (Figure 5, cycle 1). During the reusability test of this sample, the reduction of 4-NP was accomplished in only 27 min (cycle 2 shown in Figure 5). That is, half of the time needed in the cycle 1. Results similar to that presented in cycle 2 were obtained in the subsequent reusability tests (see cycles 3−5 in Figure S7).

Since the reduction reaction of 4-NP follows the Langmuir−Hinshelwood mechanism,[16,20,21] with a pseudo first-order kinetics, the expression $\ln(C_t/C_0) = \ln(A_t/A_0) = -kt$ was used to determine the reaction rate constant (k). C and A stand for the concentration and absorbance of 4-NP at a given time (t) at 400 nm, and the subscript 0 represents the time zero. The $\ln(A_t/A_0)$ versus time plots presented in Figure 5 show that the k values for the reusability cycles 2−5 vary in-between 0.09 and 0.14 s^{-1}.

The results of the first seven cycles of 4-NP degradation by the sample $CoFe_2O_4$-2.0 are presented in Figures 6 and S8. As can be noticed, the degradation of 4-NP did not take place during the first 4 cycles. However, in the 5th cycle (after about 40 min), a slow reduction of 4-NP commenced. Despite of recording the UV−vis spectra of the solution during the first 100 min, only a small amount of 4-NP was reduced in the cycle 5. In cycle 6 (after about 60 min), a higher amount of 4-NP was reduced to 4-AP; the intensity of the 400 nm absorption band decreased roughly 50%. However, as can be noticed from Figure 6, in cycle 7, the 4-NP was fully reduced within 12 min, in the presence of the catalyst. Despite that the complete degradation of 4-NP occurred only until the cycle 7 for the $CoFe_2O_4$-2.0 catalyst, the time needed for the complete reduction was much shorter (12 min) than the time needed (27 min) for the $CoFe_2O_4$-3.0 catalyst. This difference was probably due to the presence of a larger amount of Co_3O_4 in the $CoFe_2O_4$-2.0 sample (see Figure 2).

Notably, during the catalytic reduction of 4-NP by $CoFe_2O_4$-2.0, a huge amount of bubbles evolved from the surface of the particles from cycle 5; these bubbles have the ability of propelling the aggregates of particles in the solution, even upward, as shown in the video in the Supporting Information. The observation that the 4-NP degradation by $CoFe_2O_4$-2.0 starts only until the 5th cycle strongly suggests that the chemical composition of the surface of one of the impurities changed and became active for 4-NP degradation. To verify that, X-ray photoelectron spectra of the $CoFe_2O_4$-3.0 and $CoFe_2O_4$-2.0 samples were recorded before and after their utilization in 4-NP degradation. These results are discussed in the Section 2.5. Regarding the evolution of bubbles, a flame test on the gas generated at the top of the vial indicated the formation of H_2 gas due to the reaction. This agrees with the reported observation that Co_3O_4 is an efficient catalyst for $NaBH_4$ hydrolysis to generate hydrogen.[22]

The $\ln(A_t/A_0)$ versus time plots presented in Figure 6 show that the k values for the reusability cycles 7−10 vary in-

DOI: 10.1021/acsomega.9b00118
ACS Omega 2019, 4, 10129−10139

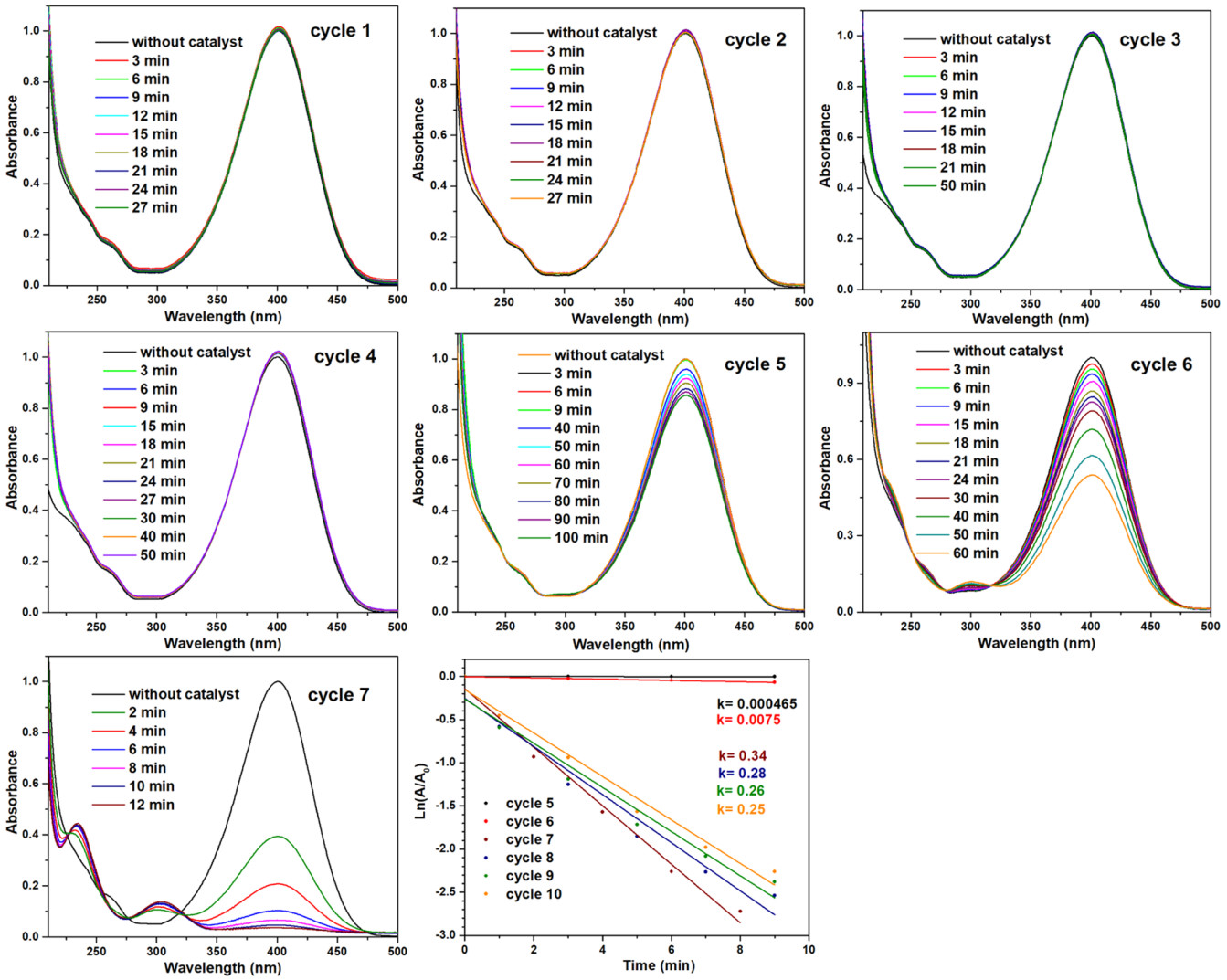

Figure 6. UV−vis absorption spectra correspond to the progressive reduction of 4-nitrophenol to 4-aminephenol using $CoFe_2O_4$-2.0 sample as a catalyst, during cycles 1−7. Apparent reaction rate constants (k) are included for the selected cycles.

between 0.25 and 0.34 s^{-1}. These k values for the $CoFe_2O_4$-2.0 catalyst are roughly twice of the same for the $CoFe_2O_4$-3.0 catalyst.

2.5. X-ray Photoelectron Spectroscopy (XPS). Figure 7a presents the XPS survey spectra for the $CoFe_2O_4$-3.0 sample before and after its use in the reduction of 4-NP. The revealed peaks correspond to the emissions from Co, Fe, and O and some of their Aüger emission lines. In addition, there appeared an emission associated to the adventitious carbon, adsorbed at the surface of the sample. In both the spectra (before and after use in 4-NP reduction), the peaks of the C 1s emission were set at 284.5 eV to compare the binding energy (BE) of the remaining orbitals with their literature-reported values. Moreover, there appeared an emission peak around 191.76 eV for the $CoFe_2O_4$-3.0/catal (used in 4-NP reduction) sample, associated to borate anions such as $[B_4O_7]^{2-}$ or BO_2^- generated by the reaction of $NaBH_4$ with the surface of cobalt ferrite, the traces of α-Fe_2O_3, or an amorphous material present in the sample. High-resolution spectra for boron and sodium elements are presented in Figure S9 of the Supporting Information. The appearance of the emission associated only to borate anions without any signal from Na^+ ions in the $CoFe_2O_4$-3.0/catal sample indicates the adsorption or formation of chemical bonds with borate anions at the surface of the catalyst.

The core-level spectra of Co $2p_{1/2}$, Co $2p_{3/2}$, Fe $2p_{1/2}$, Fe $2p_{3/2}$, O 1s, O 2s, and C 1s orbitals for the $CoFe_2O_4$-3.0 and $CoFe_2O_4$-3.0/catal samples are depicted in Figure 7b−f. Binding energy (BE) positions of the corresponding peaks are presented in Table 2. For comparison, survey and core-level spectra of these orbitals for the $CoFe_2O_4$-6.0, $CoFe_2O_4$-6.0/catal, $CoFe_2O_4$-4.5, $CoFe_2O_4$-4.5/catal, and Co_3O_4 samples are shown in Figures S10−S12. From Table 2 and the XPS peaks associated with O, Co, and Fe (Figure 7b−e), it is evident that all of the peaks in the $CoFe_2O_4$-3.0/catal sample are shifted toward higher BE compared with the same in the $CoFe_2O_4$-3.0 sample. For example, the positions of the Co $2p_{3/2}$ and Fe $2p_{3/2}$ peaks were shifted roughly about 1 eV; similarly, the positions of the peaks corresponding to O 1s and O 2s orbitals were shifted about 2 eV. The observed shifts can be attributed to a considerable increase in −OH groups bonded to the cobalt and iron cations at the surface of the sample.[23] It should be noted that the cobalt shake-up lines depicted in Figure 6b for the Co $2p_{1/2}$ and Co $2p_{3/2}$ orbitals coincide in positions for both the samples. The maximum of the Fe $2p_{3/2}$ XPS peak in Figure 7c for the sample $CoFe_2O_4$-3.0

DOI: 10.1021/acsomega.9b00118
ACS Omega 2019, 4, 10129−10139

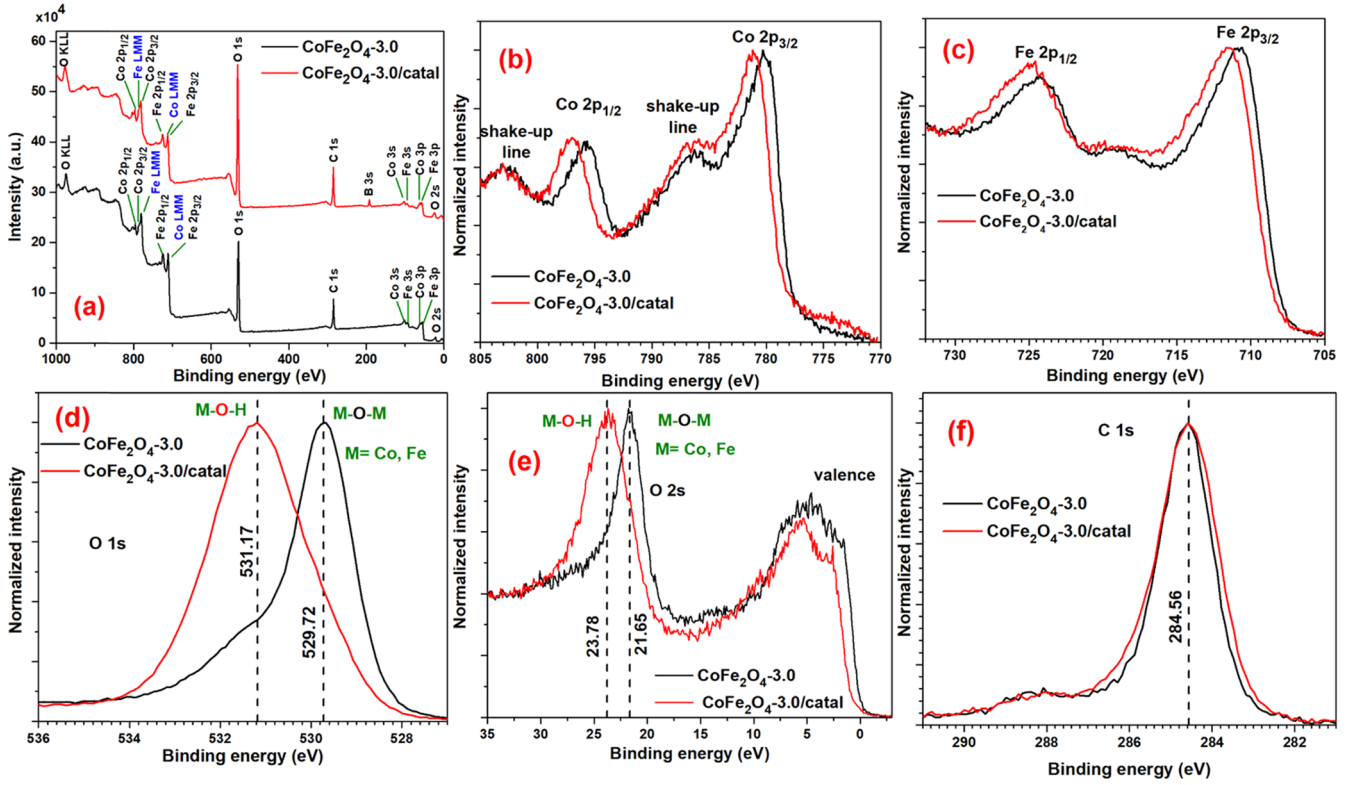

Figure 7. XPS spectra of the $CoFe_2O_4$-3.0 and $CoFe_2O_4$-3.0/catal (used in 4-NP reduction) samples. Survey (a) and high-resolution spectra of selected orbitals: (b) Co $2p_{1/2}$ and Co $2p_{3/2}$, (c) Fe $2p_{1/2}$ and Fe $2p_{3/2}$, (d) O 1s, (e) O 2s, and (f) C 1s.

Table 2. Binding Energies (BEs, eV) of the Representative XPS Emissions for the Cobalt Ferrite Samples

sample/orbital	Co $2p_{3/2}$	Co $2p_{1/2}$	Fe $2p_{3/2}$	Fe $2p_{1/2}$	O 1s	O 2s
$CoFe_2O_4$-6.0	779.77	795.46	710.56	724.01	529.62	
$CoFe_2O_4$-6.0/catal	779.37	795.27	710.13	723.75	529.26	
$CoFe_2O_4$-4.5	779.77	795.73	710.56	724.05	529.70	
$CoFe_2O_4$-4.5/catal	779.66	795.38	710.38	723.84	529.50	
$CoFe_2O_4$-3.0	780.17	795.73	710.78	724.32	529.72	21.65
$CoFe_2O_4$-3.0/catal	781.15	797.04	711.53	724.89	531.17	23.78
$CoFe_2O_4$-2.0	780.06	795.61	710.56	724.06	529.46	21.34
$CoFe_2O_4$-2.0/catal	780.91	796.87	711.49	724.89	531.14	23.56
Co_3O_4	779.42	794.76			529.22	
Co_3O_4/catal	780.57	796.53			530.86	

Table 3. Binding Energy (BE, eV), Full Width at Half-Maximum (FWHM), and Area (%) of the Components of the O 1s Peaks

	$CoFe_2O_4$-6.0			$CoFe_2O_4$-6.0/catal			$CoFe_2O_4$-4.5			$CoFe_2O_4$-4.5/catal		
peaks	BE	FWHM	area	BE	FWHM	area	BE	FWHM	area	BE	FWHM	area
peak 1	529.5	1.2	62.6	529.2	1.3	62.8	529.5	1.1	42	529.2	1	35
peak 2	529.9	1.1	25.3	530.1	1.5	12.7	529.9	1.1	42.2	529.7	1	40.5
peak 3	530.8	1.5	6.3	531.2	1.5	18.6	530.9	1.1	5.6	530.7	1.2	8.8
peak 4	531.6	1.5	5.8	532.3	1.2	5.9	531.8	1.6	10.2	531.9	1.8	15.8
	$CoFe_2O_4$-3.0			$CoFe_2O_4$-3.0/catal			$CoFe_2O_4$-2.0			$CoFe_2O_4$-2.0/catal		
peaks	BE	FWHM	area	BE	FWHM	area	BE	FWHM	area	BE	FWHM	area
peak 1	529.5	1.2	38.9	529.8	1.4	26.2	529.3	1.3	46.6	529.7	1.8	24.7
peak 2	530.0	1.2	30.5	531.1	1.5	44.1	529.8	1.6	38.25	531.1	1.8	57.3
peak 3	530.8	1.0	16.1	532.3	1.4	29.7	530.7	1.2	1.4	532.0	2.0	18.0
peak 4	531.5	1.2	14.5				531.7	1.7	13.8			

is centered at 710.8 eV, indicating that the chemical state of iron is Fe^{3+}. Interestingly, the maximum of the Fe $2p_{3/2}$ XPS peak in Figure 7c for the sample $CoFe_2O_4$-3.0/catal is located at 711.5 eV, which coincides with the reported BE for the FeOOH phase.[23] The results of the deconvolution of the spectra correspond to Co $2p_{1/2}$ orbital for the $CoFe_2O_4$-3.0

DOI: 10.1021/acsomega.9b00118
ACS Omega 2019, 4, 10129−10139

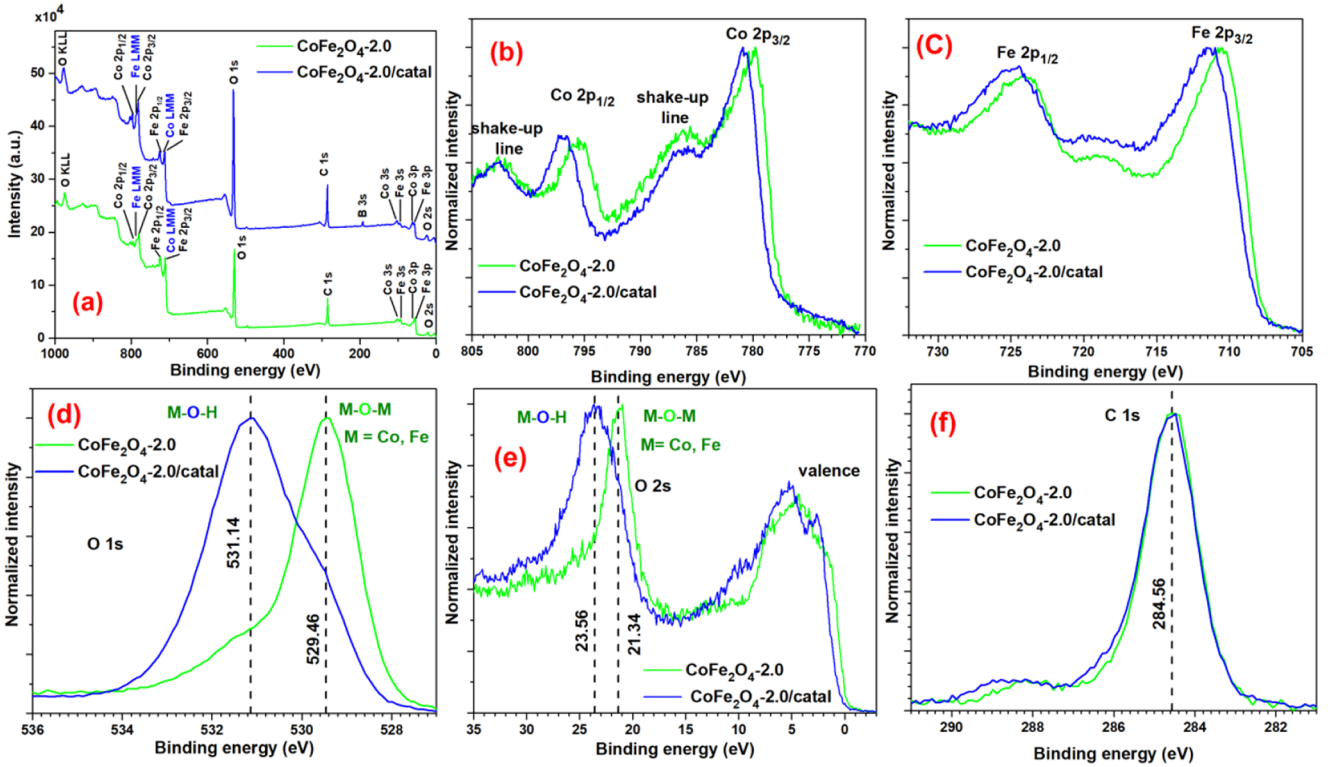

Figure 8. XPS spectra of the $CoFe_2O_4$-2.0 and $CoFe_2O_4$-2.0/catal samples. Survey (a) and high-resolution spectra of selected orbitals: (b) Co $2p_{1/2}$ and Co $2p_{3/2}$, (c) Fe $2p_{1/2}$ and Fe $2p_{3/2}$, (d) O 1s, (e) O 2s, and (f) C 1s.

and $CoFe_2O_4$-3.0/samples are presented in Figure S13 and Table S1. For comparison, the spectrum for pure cobalt ferrite (i.e., $CoFe_2O_4$-6.0) was also included. A discussion of the fit peak components of the Co $2p_{1/2}$ orbital for these samples is included in the Supporting Information.

The core-level O 1s spectrum for the $CoFe_2O_4$-3.0 and the other cobalt ferrites samples is presented in Figures 7d and S14. The deconvolution of the O 1s peak, corresponding BEs and areas (%), is presented in Figure S14 (Supporting Information) and Table 3. The deconvolution corresponding to $CoFe_2O_4$-3.0 sample generated four peaks labeled as fit peaks 1−4, two intense peaks located at 529.5 and 530.0 eV, and two low-intensity peaks located at 530.8 and 531.5 eV. Fit peaks 1 and 2 located at BEs 529.5 and 530.0 eV correspond to M−O−M {M = Co(II), Co(III), Fe(III)} chemical bonds present in the $CoFe_2O_4$ lattice. On the other hand, fit peaks 3 and 4 located at BEs 530.8 and 531.5 eV correspond to O 1s orbital in M−O−H chemical bonds. Although the area of the fit peak 1 plus fit peak 2 accounts for ∼69% of the area of O 1s peak, the area of the fit peak 3 plus fit peak 4 accounts for the remaining 31%.[23] This deconvolution allows us to conclude that on the surface of the $CoFe_2O_4$-3.0 sample, roughly 69% of the oxygens atoms is forming chemical bonds with cobalt and iron cations in $CoFe_2O_4$, α-Fe_2O_3, and roughly 31% is oxygens atoms corresponding to metal hydroxides (M−OH).

On the other hand, the O 1s emission band of the $CoFe_2O_4$-3.0/catal sample could be deconvoluted in three components (fit peaks) with binding energy positions of the component bands at 529.8, 531.1, and 532.3 eV (see Figure S14f and Table 3). Although the first component (fit peak 1 at 529.8 eV) corresponds to M−O−M {M = Co(II), Co(III), Fe(III)} chemical bonds in $CoFe_2O_4$, the second and third components (fit peaks 2 and 3 located at 531.1 and 532.3 eV) coincide with the BEs of O 1s orbitals in metallic hydroxides, for which typical reported values vary in-between 530.9 and 532 eV.[23] As the reported BE value for O 1s orbitals in borates (e.g., $Na_2B_2O_7$) is around 531.1 eV,[24] which coincides with the estimated BE value of the second component band (fit peak 2), the BE values of fit peaks 2 and 3 (531.1 and 532.3 eV) were also compared with the reported BE values for the O 1s orbital in $Co(OH)_2$ hydroxide, α-FeOOH oxohydroxide, and borate anions, which could be formed on the surface of the sample after its reaction with $NaBH_4$.

In the case of $Co(OH)_2$, the peak corresponding to the O 1s orbital was fitted by Biesinger et al., to two components with BE values 531.07 (86%) and 532.25 eV (14%).[25] These components were attributed to hydroxide (OH^-) groups and H_2O, respectively.[25] Values in parenthesis in this section correspond to the percentage of the area in the XPS peak. In the case of α-FeOOH oxohydroxide, the O 1s peak in the reported spectrum was deconvoluted in three components with binding energies 529.99 (39%), 531.20 (49%), and 532.50 eV (12%).[25] These three peaks were assigned to O^{2-} ions in the lattice, hydroxide, and H_2O, respectively. These analyses allow to state that the fit peaks shown in Figure S14f located at 529.8 eV (26.2%), 531.1 eV (44.1%), and 532.3 eV (29.7%) correspond to O^{2-} anions in the lattice of $CoFe_2O_4$, iron or cobalt hydroxide, and H_2O absorbed by the capillary condensation in the pores, respectively. These hydroxides in the $CoFe_2O_4$-3.0/catal sample were formed due to the partial reduction of the sample surface by $NaBH_4$.

Since the surface of the $CoFe_2O_4$-3.0/catal sample contains borate anions and Fe(III) cations (probably making chemical bonds between them, i.e., Fe−O−B), we compared the BE of the O 1s and B 1s orbitals in this sample with their reported BEs in iron−sodium borate glasses. The binding energies of O

DOI: 10.1021/acsomega.9b00118
ACS Omega 2019, 4, 10129−10139

1s and B 1s orbitals in a glass composed of B (21.8%), Na (12.2%), Fe (4.2%), Al (6.7%), and O (55.1%) are reported to be at 531.0 and 191.8 eV,[24] respectively. These BE values coincide well with the corresponding peak positions in the $CoFe_2O_4$-3.0/catal sample (see Figure S14f for O 1s orbital and Figure S9 for B 1s orbital), indicating a probable formation of Fe−O−B or Co−O−B chemical bonds at the surface of the cobalt ferrite sample after its utilization in 4-NP degradation.

Figure 8 depicts the survey and high-resolution XPS spectra of selected orbitals for the $CoFe_2O_4$-2.0 and $CoFe_2O_4$-2.0/catal samples. The shapes and positions of the emission bands revealed for these samples are very similar to those discussed for the $CoFe_2O_4$-3.0 and $CoFe_2O_4$-3.0/catal samples, respectively (Figure 7). In the $CoFe_2O_4$-2.0 sample, α-Fe_2O_3 and Co_3O_4 byproducts made a small contribution to the area of the O 1s peak around 530 eV (fit peak 2 in Figure S14g). The reported BE values for the O 1s orbital in α-Fe_2O_3 are ∼530,[23] 529.8,[26] and 529.88 eV.[25] On the other hand, although Dupin et al. deconvoluted the emission band of O 1s orbital emanating from Co_3O_4 in two components with BEs 529.5 (72%) and 531.5 eV (28%),[27] Biesinger et al. deconvoluted this XPS band in three components with BEs 529.95 (53%), 530.84 (41%), and 532.66 (6%).[25] Although the component at 529.95 eV was associated to O^{2-} anions in the Co_3O_4 lattice, the component at 530.84 eV was attributed to cobalt hydroxide, hydrated or defective Co_3O_4.[25] The discussion presented in the following two paragraphs further supports the claim that the surfaces of the two samples ($CoFe_2O_4$-3.0 and $CoFe_2O_4$-2.0) that exhibited a good catalytic activity after borohydride activation were partially transformed into hydroxides of cobalt and iron. For comparison, the emission band of the O 1s orbital in $CoFe_2O_4$-6.0 and $CoFe_2O_4$-4.5 is shown in Figure S14a−d (Supporting Information).

On the other hand, the Fe $2p_{3/2}$ orbital for a cobalt ferrite sample could be deconvoluted in three peaks (Figure S15 and Table S2) centered around 709.5 (35%), 710.7 (42.6%), and 712.4 (22.4%) eV. The latter peak is attributed to the LMM Aüger line of the cobalt atom, and the earlier two peaks account for the Fe^{3+} cations in the $CoFe_2O_4$ lattice.[23]

2.6. Fourier Transform Infrared Spectroscopy (FTIR). FTIR spectra of the samples before and after use in catalysis are shown in Figure S16. As can be seen in Figure S16i, the spectra of all of the samples exhibit an IR band around 3450 cm^{-1}, associated to O−H vibrations of M−O−H bonds or H_2O physisorbed at their surface. All of the samples revealed an intense IR band at 584 cm^{-1}, which has been associated to the M−O vibration in $CoFe_2O_4$.[28] An amplification (zoomed-in) of the Figure S16i in the lower frequency region is shown in Figure S16ii. As can be noticed, there appeared a week shoulder around of 530 cm^{-1} for the $CoFe_2O_4$-2.0 and $CoFe_2O_4$-2.0/catal samples that can be associated to α-Fe_2O_3 impurity.[29] In fact, the IR absorption band of the α-$Co(OH)_2$ phase has been reported to be at 634 cm^{-1}.[29] However, we could not detect any band around 634 cm^{-1} (Figures S16ii,iii) in the samples to confirm the presence of α-$Co(OH)_2$ in them either before or after utilization in 4-NP reduction.

2.7. Mechanism of 4-Nitrophenol (4-NP) Reduction. The results in the present investigation clearly demonstrate that $CoFe_2O_4$ does not reduce 4-NP. To test whether the byproduct α-Fe_2O_3 is able to reduce 4-NP, a sample of nickel ferrite was prepared using the same procedure utilizing N/G ratio 3 in the reaction mixture, to obtain α-Fe_2O_3/$NiFe_2O_4$ composite. The purpose of obtaining $NiFe_2O_4$ particles was to have a cobalt free sample. The composite was also treated thermally at 600 °C for 2 h. The XRD pattern recorded for this composite confirmed the presence of both α-Fe_2O_3 and $NiFe_2O_4$ since the XRD peaks coincide in position and intensity with their standard values (PDFs 04-006-6579 and 00-054-0964, Figure S17). Testing this α-Fe_2O_3/$NiFe_2O_4$ composite in 4-NP degradation revealed its inability for 4-NP reduction (results not presented); confirming that hematite (α-Fe_2O_3) is not active for the degradation of 4-NP. Therefore, the species responsible for 4-NP degradation observed for the $CoFe_2O_4$-3.0 sample are small cobalt nanoparticles, which were detected in its XRD spectrum (Figure 2). Previous studies have also reported the reduction of 4-NP with cobalt nanoparticles.[30,31] Note that the diffraction peak located at 44.30° persists in the $CoFe_2O_4$-3.0 sample even after its use in catalysis (Figure 2). In fact, cobalt NPs are the known active species for the reduction of 4-NP, which can be formed in solution combustion reactions when the N/G ratio is low.[32] For instance, mixing $Co(NO_3)_2$ and glycine at a N/G ratio of 0.75 in the solution combustion process, Khort et al. obtained a mixture of Co (6%), CoO (56%), and Co_3O_4 (38%).[32] On the other hand, 4-NP reduction ability of α-$Co(OH)_2$ has been demonstrated by Khan et al. for a sample containing α-$Co(OH)_2$, although the signal/noise ratio of the X-ray diffraction peaks of this phase was extremely low.[33] Finally, the possible contributions of amorphous $CoFe_2O_{3.66}$ and amorphous $Fe_{40}Co_{60}O_x$ phases in 4-NP reduction cannot be discarded as both of them have been utilized successfully in the catalytic oxidation of water and oxygen reduction reactions revealing superior performances than their respective crystalline counterparts.[34,35]

In the case of the $CoFe_2O_4$-2.0 sample, the Co_3O_4 byproduct is responsible for 4-NP reduction. Some previous works also concluded that Co_3O_4 reduces 4-NP to 4-AP, which further supports the results found in this work.[27,36−38] Based on the XPS results discussed in this work and the fact that the 4-NP reduction started only until cycle 5, the possible mechanism of 4-NP reduction is depicted schematically in Figure 9. In step 1, the cobalt−water moieties at the surface of the Co_3O_4 are transformed to CoO(OH) through the reaction among the hydride anion (H^-) provided by the NBH_4 and the chemisorbed H_2O, followed by redox reactions. In other words, the Co(III) cations at the surface of the Co_3O_4 particles are reduced by $NaBH_4$ to Co(II), as indicated in step 1. This could be possible as the redox potential of $NaBH_4$ is high (approximately −0.6 V).[39] Also, the nitro group ($-NO_2$) of 4-nitrophenolate ion bonds to the cobalt cations in the Co_3O_4. Then, in the step 2, a highly reactive hydride anion (H^-) is transferred from $NaBH_4$ to the nitrogen atom in the 4-nitrophenolate ion and, simultaneously, occurs in the N−O single bond breaking. After that a second H^- anion reacts with the N═O moiety and, hence, induces the N═O bond cleavage, generating 4-(hydroxylamino)phenol. In step 3, the 4-(hydroxylamino)phenol is reduced to 4-AP in the presence of H_2.[40] Finally, the remaining B−H bonds are hydrolyzed with water to generate H_2 and Co−O−$B(OH)_3$ species at the surface of the reduced Co_3O_4 (step 4).

3. CONCLUSIONS

In summary, we demonstrate the fabrication of both phase pure and impure $CoFe_2O_4$ particles through the solution combustion process by controlling the nitrate ions/glycine (N/G) ratio in the reaction. Although phase pure $CoFe_2O_4$

DOI: 10.1021/acsomega.9b00118
ACS Omega 2019, 4, 10129−10139

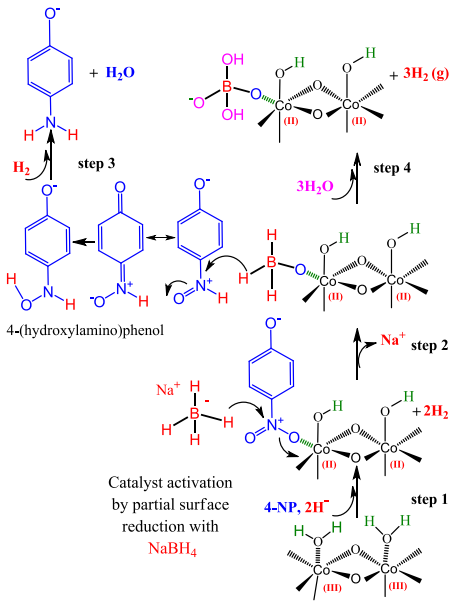

Figure 9. Proposed mechanism of 4-nitrophenol (4-NP) reduction inspired from Figure 8 in ref 41.

particles of sub-micrometer sizes can be fabricated using N/G ratios of 6.0 or 4.5 in the reaction mixture, at N/G ratio 3.0, $CoFe_2O_4$ particles with traces of α-Fe_2O_3 and cobalt are generated. On the other hand, at N/G ratio 2.0, $CoFe_2O_4$ particles are generated along with large quantities of α-Fe_2O_3 and traces of Co_3O_4 byproducts. The generation of the intense flame and high temperature during the solution combustion process at lower N/G ratios such as 3.0 and 2.0 induces the formation of bigger particles (>400 nm) in the samples. Although phase pure $CoFe_2O_4$ particles are not active as catalysts for the reduction of 4-NP, the Co_3O_4 formed over $CoFe_2O_4$ (in the sample synthetized with a N/G ratio of 2.0) is capable of reducing 4-nitrophenol (4-NP) to 4-aminophenol (4-AP) in the presence of $NaBH_4$. The required times for the complete reduction of 4-NP for the $CoFe_2O_4$ samples prepared at N/G ratios 3.0 and 2.0 were 27 and 12 min, respectively. We demonstrate that the Co_3O_4 supported on FeO_2O_4 particles is a low-cost and magnetically separable catalyst useful for the degradation of 4-NP. However, it requires a prolonged (~4 h) activation in the aqueous solution of $NaBH_4$. 4-NP starts to be reduced only until a considerable amount of bubbles are generated at the surface of the catalyst. At the surface of the catalytically active cobalt ferrite samples, oxides {M−O−M; M = Co(II,III), Fe(III)} are reduced to hydroxides by $NaBH_4$. Borate anions generated from the $NaBH_4$ oxidation in water chemically bond to the surface of the cobalt ferrite.

4. EXPERIMENTAL SECTION

4.1. Reagents and Equipment. The reagents used for the synthesis of cobalt ferrite particles and 4-NP degradation tests performed in this work were cobalt nitrate hexahydrate ($Co(NO_3)_2{\cdot}6H_2O$, Sigma, 99.99%), iron nitrate nonahydrate ($Fe(NO_3)_3{\cdot}9H_2O$, Sigma, 99.99%), glycine (H_2NCH_2COOH, Aldrich, 99%), diluted nitric acid (HNO_3, J.T. Baker, 66%), 4-nitrophenol ($O_2NC_6H_4OH$, Sigma, ≥99%), sodium borohydride ($NaBH_4$, Sigma, 99%). All of the reagents were utilized as received, without further processing or purification. Deionized water from a Millipore water purification system (ρ > 10^{18} Ohm.cm) was utilized to dissolve the reagents and the 4-nitrophenol to carry out its catalytic tests. XRD patterns of the samples shown in Figure 1 were recorded in a Bruker D8 Discover X-ray diffractometer, equipped with a LynxEye detector, using an acrylic sample holder. The spectra were recorded at 0.02°/step and 0.3 s acquisition time at each point. Fluorescence was diminished in the diffractogram by adjusting the discrimination lower level at 0.18 V in the detector of the equipment.

Also, the XRD patterns shown in Figure 2 in the range of 2θ = 30−53° were recorded in a Bruker D2 Phaser diffractometer equipped with a LynxEye detector, using a low-noise silicon sample holder. The measurement conditions in the D2 diffractometer were 0.01°/step and 3 s acquisition time at each step. The fluorescence was not removed. A JEOL JSM-7800F field-emission scanning electron microscope (SEM) operating at 3.0 kV was utilized for the morphology evaluation of the particles. Nitrogen adsorption−desorption isotherms of the $CoFe_2O_4$ samples were measured at 77 K using a texture analyzer instrument (BELSORP Mini-II System). The outgassing of the samples was done at 10 Pa pressure and 300 °C temperature for 12 h. For catalytic tests, a Shimadzu UV-3101PC double-beam spectrophotometer was utilized. An X-ray photoelectron spectrometer (XPS, Thermo Scientific) with Al Kα (1486.6 eV) radiation source was utilized to analyze the surface composition of the composites. The deconvolution of the O 1s core-level emission bands was performed using Pseudo-Voight2 functions with 70% Gaussian and 30% Lorentzian components, after subtracting the Shirley-type background. FTIR spectra were recorded in a Perkin-Elmer Frontier spectrometer over the cold-pressed pellets made of 2% ferrite samples in 98% dry KBr powder. ATR-FTIR spectra of the powder samples were recorded in a Perkin-Elmer Spectrum One spectrometer, using the GladiATR accessory (PIKE Technologies).

4.2. Synthesis of Cobalt Ferrites. In a typical synthesis of $CoFe_2O_4$ particles, 3 mmol of $Co(NO_3)_2{\cdot}6H_2O$, 6 mmol of $Fe(NO_3)_3{\cdot}9H_2O$, and 12.9 mmol of glycine were dissolved in 70 mL of deionized water in a 600 mL beaker under magnetic stirring. Then, 1 mL of HNO_3 was added to the mixture, similar to our previously reported work.[16] The volume of HNO_3 was varied to attain nitrate ions/glycine (N/G) ratios of 6, 4.5, 3, and 2. The prepared mixture solutions were heated at 85 °C (under magnetic stirring) to evaporate the water. On evaporating all of the water from the mixture, an ignition occurred, and in some cases, a flame inside the beaker could be observed. The combustion reaction produced a black powder. The powder samples obtained in the solution combustion process were annealed in an air atmosphere at 600 °C for 2 h, inside a tubular furnace, using a heating ramp of 2 °C/min. A similar procedure was adapted for the synthesis of Co_3O_4 particles with a (N/G) ratio of 2.

4.3. Catalytic Reduction of 4-Nitrophenol (4-NP) to 4-Aminophenol. 4-NP solution (4 mL, 0.2 mM) was mixed with 12 mL of deionized water in a 35 mL vial. Then, 15 mg of $NaBH_4$ was added to the solution, and its UV−vis absorption spectrum was recorded. After that 10 mg of the cobalt ferrite sample was added to the solution under shaking. The absorption spectra of the reaction mixture were recorded every 2 or 3 min, isolating the catalyst from the reaction mixture by a bar magnet. After the first cycle of the catalytic test, the sample was held at the bottom of the vial with a magnet, and the liquid (supernatant) inside the vial was removed (discarded). Then, another 4 mL of 4-NP solution

DOI: 10.1021/acsomega.9b00118
ACS Omega 2019, 4, 10129−10139

(0.2 mM) was mixed with 12 mL of deionized water and 15 mg of $NaBH_4$. After that a UV−vis absorption spectrum was recorded. Finally, the solution was added to the 35 mL vial containing the used catalyst, and the UV−vis absorption spectra were recorded on the aliquots extracted from the reaction mixture every 2 or 3 min.

■ ASSOCIATED CONTENT

Supporting Information

The Supporting Information is available free of charge on the ACS Publications website at DOI: 10.1021/acsomega.9b00118.

Elemental mapping of cobalt, iron, and oxygen in the cobalt ferrite samples; UV−vis absorption spectra corresponding to reusability tests of the $CoFe_2O_4$-3.0 and $CoFe_2O_4$-2.0 samples for the reduction of 4-nitrophenol to 4-aminephenol; high-resolution XPS spectra of B 1s, Na 1s, O 1s, Co $2p_{3/2}$ orbitals for the $CoFe_2O_4$-3.0/catal and $CoFe_2O_4$-2.0/catal samples; XRD pattern of Co_3O_4 particles and α-Fe_2O_3/$NiFe_2O_4$ composite synthesized at a N/G ratio of 2 (PDF)

Reduction of 4-nitrophenol to 4-aminophenol with $NaBH_4$ in presence of $CoFe_2O_4$ particles with impurities of Co_3O_4 and Fe_2O_3 (MPG)

■ AUTHOR INFORMATION

Corresponding Author

*E-mail: upal@ifuap.buap.mx.

ORCID

Umapada Pal: 0000-0002-5665-106X

Notes

The authors declare no competing financial interest.

■ ACKNOWLEDGMENTS

J.-L.O.-Q. thanks SEP, Mexico, for the postdoctoral fellowship offered through PRODEP Grant 511-6/17-9449, and to CONACyT-SENER for the postdoctoral fellowship. Partial financial helps offered by the VIEP-BUAP, and CONACyT (Grants # 100236944-BUAP2018 & INFR-2014-02-23053), Mexico are acknowledged.

■ REFERENCES

(1) Budanov, M. A.; Lefedova, O. V.; Ulitin, M. V.; Kha, N. T. T. Features of the Phenylhydroxylamine Catalytic Hydrogenation in Water Solutions of 2-Propanole on Skeletal Nickel. *Russ. J. Phys. Chem. A* **2010**, *84*, 1901−1904.

(2) Formenti, D.; Ferretti, F.; Scharnagl, F. K.; Beller, M. Reduction of Nitro Compounds Using 3d-Non-Noble Metal Catalysts. *Chem. Rev.* **2019**, *119*, 2611−2680.

(3) Xiong, Z.; Zhang, H.; Zhang, W.; Lai, B.; Yao, G. Removal of Nitrophenols and Their Derivatives by Chemical Redox: A Review. *Chem. Eng. J.* **2019**, *359*, 13−31.

(4) Aditya, T.; Pal, A.; Pal, T. Nitroarene Reduction: A Trusted Model Reaction to Test Nanoparticle Catalysts. *Chem. Commun.* **2015**, *51*, 9410−9431.

(5) Li, H.; Han, L.; Cooper-White, J.; Kim, I. Palladium Nanoparticles Decorated Carbon Nanotubes: Facile Synthesis and Their Applications as Highly Efficient Catalysts for the Reduction of 4-Nitrophenol. *Green Chem.* **2012**, *14*, 586−591.

(6) Corma, A.; Serna, P.; Concepción, P.; Calvino, J. J. Transforming Nonselective into Chemoselective Metal Catalysts for the Hydrogenation of Substituted Nitroaromatics. *J. Am. Chem. Soc.* **2008**, *130*, 8748−8753.

(7) Shu, Y.; Chan, H. C.; Xie, L.; Shi, Z.; Tang, Y.; Gao, Q. Bimetallic Pt-Sn Nanoparticles on Hydrogenated MoO_x for the Selective Hydrogenation of Functionalized Nitroarenes. *ChemCatChem* **2017**, *9*, 4199−4205.

(8) Zhang, Y.; Fang, H.; Zhang, Y.; Wen, M.; Wu, D.; Wu, Q. Active Cobalt Induced High Catalytic Performances of Cobalt Ferrite Nanobrushes for the Reduction of p-Nitrophenol. *J. Colloid Interface Sci.* **2019**, *535*, 499−504.

(9) Huang, Y.; Sun, X.; Huo, S.; Li, Y.; Zhong, C. Core-Shell Dual-MOF Heterostructures Derived Magnetic CoFe2O4/CuO (Sub) Microcages with Superior Catalytic Performance. *Appl. Surf. Sci.* **2019**, *466*, 637−646.

(10) Gao, Q.; Sun, Z. Facile Fabrication of Uniform MFe_2O_4 (M = Co, Ni, Cu) Hollow Spheres and Their Recyclable Superior Catalytic Activity Towards 4-Nitrophenol Reduction. *J. Nanosci. Nanotechnol.* **2018**, *18*, 5645−5653.

(11) Naghshbandi, Z.; Arsalani, N.; Sadegh, M.; Geckeler, K. E. Novel Synthesis of Magnetic and Photoluminescent Graphene Quantum Dots/MFe_2O_4 (M = Ni, Co) Nanocomposites for Catalytic Application. *Appl. Surf. Sci.* **2018**, *443*, 484−491.

(12) Nasrollahzadeh, M.; Bagherzadeh, M.; Karimi, H. Preparation, Characterization and Catalytic Activity of $CoFe_2O_4$ Nanoparticles as a Magnetically Recoverable Catalyst for Selective Oxidation of Benzyl Alcohol to Benzaldehyde and Reduction of Organic Dyes. *J. Colloid Interface Sci.* **2016**, *465*, 271−278.

(13) Song, Q.; Zhang, Z. J. Shape Control and Associated Magnetic Properties of Spinel Cobalt Ferrite Nanocrystals. *J. Am. Chem. Soc.* **2004**, *126*, 6164−6168.

(14) Wu, G.; Liang, X.; Zhang, L.; Tang, Z.; Al-mamun, M.; Zhao, H.; Su, X. Fabrication of Highly Stable Metal Oxide Hollow Nanospheres and Their Catalytic Activity toward 4-Nitrophenol Reduction. *ACS Appl. Mater. Interfaces* **2017**, *9*, 18207−18214.

(15) Martinson, K. D.; Cherepkova, I. A.; Sokolov, V. V. Formation of Cobalt Ferrite Nanoparticles via Glycine-Nitrate Combustion and Their Magnetic Properties. *Glass Phys. Chem.* **2018**, *44*, 21−25.

(16) Ortiz-Quiñonez, J.-L.; Pal, U.; Villanueva, M. S. Structural, Magnetic, and Catalytic Evaluation of Spinel Co, Ni, and Co−Ni Ferrite Nanoparticles Fabricated by Low-Temperature Solution Combustion Process. *ACS Omega* **2018**, *3*, 14986−15001.

(17) Kazemi, M.; Ghobadi, M.; Mirzaie, A. Cobalt Ferrite Nanoparticles ($CoFe_2O_4$ MNPs) as Catalyst and Support: Magnetically Recoverable Nanocatalysts in Organic Synthesis. *Nanotechnol. Rev.* **2018**, *7*, 43−68.

(18) Sing, K. S. W.; Everett, D. H.; Haul, R. A. W.; Moscou, L.; Pierotti, R. A.; Rouquérol, J.; Siemieniewska, T. Reporting Physisorption Data for Gas/Solid Systems with Special Reference to the Determination of Surface Area and Porosity. *Pure Appl. Chem.* **1985**, *57*, 603−619.

(19) Brunauer, S.; Emmett, P. H.; Teller, E. Adsorption of Gases in Multimolecular Layers. *J. Am. Chem. Soc.* **1938**, *60*, 309−319.

(20) Wunder, S.; Lu, Y.; Albrecht, M.; Ballau, M. Catalytic Activity of Faceted Gold Nanoparticles Studied by a Model Reaction: Evidence for Substrate-Induced Surface Restructuring. *ACS Catal.* **2011**, *1*, 908−916.

(21) Wunder, S.; Polzer, F.; Lu, Y.; Mei, Y.; Ballauff, M. Kinetic Analysis of Catalytic Reduction of 4-Nitrophenol by Metallic Nanoparticles Immobilized in Spherical Polyelectrolyte Brushes. *J. Phys. Chem. C* **2010**, *114*, 8814−8820.

(22) Simagina, V. I.; Komova, O. V.; Ozerova, A. M.; Netskina, O. V.; Odegova, G. V.; Kellerman, D. G.; Bulavchenko, O. A.; Ishchenko, A. V. Cobalt Oxide Catalyst for Hydrolysis of Sodium Borohydride and Ammonia Borane. *Appl. Catal., A* **2011**, *394*, 86−92.

(23) Moulder, J. F.; Stickle, W. F.; Sobol, P. F.; Kenneth, B. D. *Handbook of X-Ray Photoelectron Spectroscopy*, 1st ed.; Perkin-Elmer Corporation: Eden Prairie, 1992.

(24) Khattak, G. D.; Salim, M. A.; Wenger, L. E.; Gilani, A. H. X-Ray Photoelectron Spectroscopy (XPS) and Magnetization Studies of Iron-Sodium Borate Glasses. *J. Non-Cryst. Solids* **1999**, *244*, 128−136.

DOI: 10.1021/acsomega.9b00118
ACS Omega 2019, 4, 10129−10139

(25) Biesinger, M. C.; Payne, B. P.; Grosvenor, A. P.; Lau, L. W. M.; Gerson, A. R.; Smart, C. S. R. Resolving Surface Chemical States in XPS Analysis of First Row Transition Metals, Oxides and Hydroxides: Cr, Mn, Fe, Co and Ni. *Appl. Surf. Sci.* **2011**, *257*, 2717−2730.
(26) Heuer, J. K.; Stubbins, J. F. An XPS Characterization of $FeCO_3$ Films from CO_2 Corrosion. *Corros. Sci.* **1999**, *41*, 1231−1243.
(27) Dupin, J.; Gonbeau, D.; Vinatier, P.; Levasseur, A. Systematic XPS Studies of Metal Oxides, Hydroxides and Peroxides. *Phys. Chem. Chem. Phys.* **2000**, *2*, 1319−1324.
(28) Kumar, P. R.; Kollu, P.; Santhosh, C.; Rao, E.-V.; Kim, D. K.; Grace, A. N. Enhanced Properties of Porous $CoFe_2O_4$−reduced Graphene Oxide Composites with Alginate Binders for Li-Ion Battery Applications. *New J. Chem.* **2014**, *38*, 3654−3661.
(29) Li, R.; Hu, Z.; Shao, X.; Cheng, P.; Li, S.; Yu, W.; Lin, W.; Yuan, D. Large Scale Synthesis of NiCo Layered Double Hydroxides for Superior Asymmetric Electrochemical Capacitor. *Sci. Rep.* **2016**, *6*, No. 18737.
(30) Mondal, A.; Mondal, A.; Adhikary, B.; Mukherjee, D. K. Cobalt Nanoparticles as Reusable Catalysts for Reduction of 4-Nitrophenol under Mild Conditions. *Bull. Mater. Sci.* **2017**, *40*, 321−328.
(31) Du, M.; Liu, Q.; Huang, C.; Qiu, X. One-Step Synthesis of Magnetically Recyclable Co@BN Core−shell Nanocatalysts for Catalytic Reduction of Nitroarenes. *RSC Adv.* **2017**, *7*, 35451−35459.
(32) Khort, A.; Podbolotov, K.; Serrano-García, R.; Gun'Ko, Y. One-Step Solution Combustion Synthesis of Cobalt Nanopowder in Air Atmosphere: The Fuel Effect. *Inorg. Chem.* **2018**, *57*, 1464−1473.
(33) Khan, M. N.; Bashir, O.; Khan, T. A.; Al-Thabaiti, S. A.; Khan, Z. Catalytic Activity of Cobalt Nanoparticles for Dye and 4-Nitro Phenol Degradation: A Kinetic and Mechanistic Study. *Int. J. Chem. Kinet.* **2017**, *49*, 438−454.
(34) Indra, A.; Menezes, P. W.; Sahraie, N. R.; Bergmann, A.; Das, C.; Tallarida, M.; Schmeißer, D.; Strasser, P.; Driess, M. Unification of Catalytic Water Oxidation and Oxygen Reduction Reactions: Amorphous Beat Crystalline Cobalt Iron Oxides. *J. Am. Chem. Soc.* **2014**, *136*, 17530−17536.
(35) Smith, R. D. L.; Prévot, M. S.; Fagan, R. D.; Trudel, S.; Berlinguette, C. P. Water Oxidation Catalysis: Electrocatalytic Response to Metal Stoichiometry in Amorphous Metal Oxide Films Containing Iron, Cobalt, and Nickel. *J. Am. Chem. Soc.* **2013**, *135*, 11580−11586.
(36) Chen, H.; Yang, M.; Tao, S.; Chen, G. Oxygen Vacancy Enhanced Catalytic Activity of Reduced Co_3O_4 towards p-Nitrophenol Reduction. *Appl. Catal., B* **2017**, *209*, 648−656.
(37) Mogudi, B. M.; Ncube, P.; Meijboom, R. Catalytic Activity of Mesoporous Cobalt Oxides with Controlled Porosity and Crystallite Sizes: Evaluation Using the Reduction of 4-Nitrophenol. *Appl. Catal., B* **2016**, *198*, 74−82.
(38) Al Nafiey, A.; Addad, A.; Sieber, B.; Chastanet, G.; Barras, A.; Szunerits, S.; Boukherroub, R. Reduced Graphene Oxide Decorated with Co_3O_4 Nanoparticles (RGO-Co_3O_4) Nanocomposite: A Reusable Catalyst for Highly Efficient Reduction of 4-Nitrophenol, and Cr(VI) and Dye Removal from Aqueous Solutions. *Chem. Eng. J.* **2017**, *322*, 375−384.
(39) Connelly, N. G.; Geiger, W. E. Chemical Redox Agents for Organometallic Chemistry. *Chem. Rev.* **1996**, *96*, 877−910.
(40) Corma, A.; Concepción, P.; Serna, P. A Different Reaction Pathway for the Reduction of Aromatic Nitro Compounds on Gold Catalysts. *Angew. Chem., Int. Ed.* **2007**, *46*, 7266−7269.
(41) Hunter, B. M.; Gray, H. B.; Müller, A. M. Earth-Abundant Heterogeneous Water Oxidation Catalysts. *Chem. Rev.* **2016**, *116*, 14120−14136.

DOI: 10.1021/acsomega.9b00118
ACS Omega 2019, 4, 10129−10139